Journal of Applied Polymer Science

Novel magnetic polyamic hydrazide nanocomposite: Preparation, characterization, and application for the removal of Cd^{2+} and Pb^{2+} from industrial wastes

Kiomars Zargoosh, Hossein Habibi, Amir Abdolmaleki, Kourosh Firouz
Department of Chemistry, Isfahan University of Technology, Isfahan, Iran
Correspondence to: K. Zargoosh (E-mail: Kiomarszargoosh@cc.iut.ac.ir)

ABSTRACT: In this work, a novel polymer polyamic hydrazide (PAH) was synthesized via the reaction of terephthalohydrazide with pyromelitic dianhydride. The obtained PAH was characterized with nuclear magnetic resonance (NMR) spectroscopy, Fourier transform infrared (FT-IR) spectroscopy and elemental analysis. Finally, a novel magnetic nanocomposite was prepared by immobilization of PAH on the Fe_3O_4 nanoparticles in water. The prepared magnetic nanocomposite was successfully used for selective removal of Pb^{2+} and Cd^{2+} ions from industrial wastes and the effects of affecting parameters on the adsorption capacity of the magnetic nanocomposite adsorbent for the removal of Pb^{2+} and Cd^{2+} from model aqueous solutions were investigated. The maximum adsorption capacities of Pb^{2+} and Cd^{2+} were found to be 138.9 and 103.1 mg g^{-1}, respectively. The kinetics and mechanism of the adsorption of Pb^{2+} and Cd^{2+} on the surface of the prepared nanocomposite were studied and it was found that complex formation between active sites of the surface of the nanocomposite and metal ions is the possible mechanism for adsorption of metal cations. © 2015 Wiley Periodicals, Inc. J. Appl. Polym. Sci. **2015**, *132*, 42538.

KEYWORDS: adsorption; applications; composites

Received 6 January 2015; accepted 25 May 2015
DOI: 10.1002/app.42538

INTRODUCTION

Nanocomposites are the product of conscious designing, synthesis, and modification of the nanosized materials for pre-defined applications. Today, nanocomposites have wide applications in different areas such as preparation of chemical and biochemical sensors,[1,2] removal of inorganic and organic pollutants from environmental samples,[3–5] drug targeting,[6,7] hyperthermia therapy,[8] fuel cell constructing,[9] preparation of supercapacitors[10] and catalysis of chemical reactions.[11,12] Among the different types of nanocomposites, magnetic nanocomposites have been proposed by several researchers for the removal or isolation of pollutants from industrial wastes and environmental waters, because magnetic nanocomposites can be easily separated from solutions.[13–15] However, there are some problems that limited the practical applicability of the magnetic nanocomposites for the removal of toxic substances from real samples such as industrial wastes. For example, Fe_3O_4 nanoparticles must be covered with a shell of polyacrylic acid for additional modification. Solubility of polyacrylic acid in water introduces some degree of instability in the structure of magnetic nanocomposites. In addition, lack of selectivity can significantly reduce the adsorption capacity of the magnetic nanocomposites during treatment of real samples containing considerable amounts of different pollutants.

Widely used magnetic nanocomposites for separation of pollutants from aqueous solutions contain a magnetic part (metal, alloy or metal oxide) and active sites for effective interaction with contaminant particles (ions, molecules, or radicals). Chemical and physical properties (such as charge, size, and bonding ability) of the pollutant particles determine the chemical structures of the active sites.[16,17] For the removal of heavy metal ions from aqueous solutions, commonly, the active sites include the functional groups such as carboxyl, hydroxyl, amine, sulfide, thiol, and amide.[18,19] It have been demonstrated that nanocomposites containing active sites with soft-donor groups such as amine and sulfide are one of the best choices for effective removal of heavy metal ions from aqueous solutions.[16,17] These nanoadsorbents form reversible complexes with heavy metal cations and, hence, can remove them in the presence of interfering species such as phosphate anions and alkaline earth metal cations.[16,18] Interfering ions can occupy active sites of the adsorbents and, hence, reduce their capacity for the removal of target ions. These interferences are especially important in heavy metal removal of real samples containing large amounts of alkaline and alkaline earth metal cations.

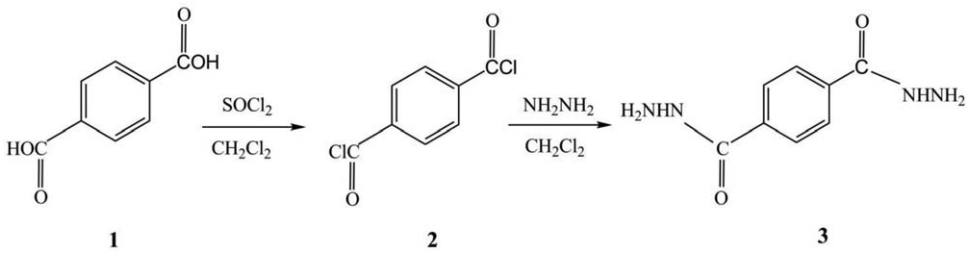

Scheme 1. Synthesis of terephthalohydrazide.

The aim of this work is to prepare stable and reusable magnetic nanocomposite for the removal of Pb^{2+} and Cd^{2+} ions from industrial wastes in the presence of considerable amounts of other cations. The magnetic nanocomposite was prepared by synthesis of a novel polymer, polyamic hydrazide (PAH), and immobilization of it on the magnetic Fe_3O_4 nanoparticles. Then, the structural and adsorption characteristics of the PAH modified magnetic nanocomposite, Fe_3O_4@PAH, were investigated with different techniques. Finally, Fe_3O_4@PAH magnetic nanocomposite was successfully used for the removal of Pb^{2+} and Cd^{2+} ions from model aqueous solutions and industrial wastes. In addition, adsorption mechanism, adsorption kinetics and adsorption isotherms were investigated.

MATERIALS AND METHODS

Materials

All chemicals and reagents were analytical grade. Hydrochloric acid (HCl), sodium hydroxide (NaOH), iron(III) chloride ($FeCl_3{\cdot}6H_2O$), iron(II) chloride ($FeCl_2{\cdot}4H_2O$), cadmium chloride ($CdCl_2{\cdot}2.5\ H_2O$), lead nitrate ($Pb(NO_3)_2$) were purchased from Merck. Pyromelitic dianhydride (PMD), dimethyl sulfoxide (DMSO), acetone, ethanol, hydrazine hydrate, terephthalic acid, and thionyl chloride were purchased from Sigma-Aldrich. Doubly distilled deionized water was used throughout.

Apparatus

The reactions were occurred on a MISONIX ultrasonic liquid processor, XL-2000 SERIES. Ultrasonic irradiation was carried out with the horn probe of the ultrasonic immersed directly in the solution mixture with frequency 2.25×10^4 Hz and power 100 W. A Canon-Fenske viscometer was used for the determination of the inherent viscosity of the synthesized PAH polymer. Fourier transform infrared (FT-IR) spectra were obtained with a Bruker model Eqvinox 55 LS101 FT-IR spectrophotometer. X-ray diffraction (XRD) measurements were carried using a Siemens D-5000 X-ray diffractometer (Germany) with Cu Kα radiation. A transmission electron microscopy (TEM) analyzer, Philips CM 120, was used for investigating the morphology and dispersity of the prepared Fe_3O_4 nanoparticles. Field-emission scanning electron microscopy (FE-SEM) S-4160 Hitachi (Japan) was used to investigate the morphology and size distribution of the prepared nanocomposite. Low temperature N_2-adsorption measurements, Brunauer–Emmett–Teller (BET) measurements, were recorded on a Quantachrome Autosorb-1 system. Samples pretreated by heating at 353 K under vacuum for 2 h were used to determine the surface areas at 77 K using N_2 as the adsorbate and He as the carrier gas. A Perkin-Elmer 2380-Waltham flame atomic absorption spectrophotometer (FAAS) was used for the determination of the metal ions concentration. A Jenway (USA) model 3020 pH meter with a combined glass electrode was used after calibration against standard Merck buffers for pH determinations. A totally glass Fisons (UK) double distiller was used for preparation of doubly distilled water.

Synthesis of Fe_3O_4 Magnetic Nanoparticles

Fe_3O_4 magnetic nanoparticles (MNPs) were prepared by a chemical coprecipitation method.[20] Briefly, $FeCl_3$ (10.8 g) and $FeCl_2$ (4.0 g) were dissolved in degassed hydrochloric acid (2 mol L^{-1}, 50 mL) in a flask at room temperature under sonication. All the solutions were degassed using a vacuum pump and filled with nitrogen gas. The contents of the flask were stirred for 10 min before aqueous ammonia (28%, 80 mL) was injected slowly over 1 h into the mixture under nitrogen while stirring at room temperature. The resulting solid was rinsed with deionized water (3×60 mL) and resuspended in deionized water (100 mL). The obtained Fe_3O_4 MNPs were rinsed with ethanol several times and dried at 60°C under vacuum for 3 h.

Synthesis of Terephthaloyl Dichloride

A previously reported method with some modifications was used for the preparation of terephthaloyl dichloride.[21] Hydrazine was used instead of benzhydrazide and the temperature of reaction was lowered to 60°C. The 25 mL side-arm flask with a magnetic stirring bar was charged with terephthalic acid 1 (0.166 g: 1.0 mmol), thionyl chloride (3 mL: 20 mmol), CH_2Cl_2 (5 mL) and dimethylformamide (0.5 mL), and then refluxed for 12 h at 60°C. After the removal of the solvent under reduced pressure, the resulting terephthaloyl dichloride 2 was dried under nitrogen atmosphere and used in the next reaction. The mass of the prepared terephthaloyl dichloride was 0.199 g (yield 98%).

Synthesis of Terephthalohydrazide

Terephthalohydrazide 3 (TPH) was synthesized via the reaction of terephthaloyl dichloride (0.203 g : 1 mmol) and hydrazine hydrate (0.66 mL : 10 mmol) in dichloromethane (10 mL) as solvent (see Scheme 1).[21] The mixture was refluxed for 14 h at room temperature. The obtained precipitate (TPH) was collected by filtration and washed thoroughly with cold water and dried under vacuum at room temperature for 72 h. The mass of the prepared TPH was 0.181 g (yield 93%).

Synthesis of Polyamic Hydrazide

In 25 mL side-arm flask with a magnetic stirring bar TPH (0.194 g: 1.0 mmol) was dissolved in 3 mL DMSO. Then, the

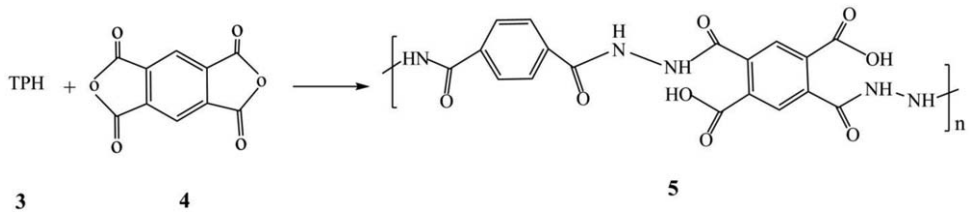

Scheme 2. Synthesis of polyamic hydrazide (PAH).

obtained solution was degassed using a vacuum pump and filled with nitrogen gas. Under nitrogen atmosphere, the temperature of the solution was cooled down to 0°C and PMD 4 (0.218 g: 1 mmol) was slowly (during 15 min) added to the solution. The resulting solution was stirred for 2 h under nitrogen atmosphere at 0°C. Finally, the light-yellow polymer was precipitated by addition of excess amount of water to the solution (see Scheme 2). The mass of the obtained PAH 5 was 0.292 g (yield 71%).

Preparation of Magnetic Nanocomposite

Under nitrogen atmosphere, the Fe_3O_4 MNPs (0.1 g) were ultrasonicated for 30 min in 10 mL of water to obtain dispersed MNPs. Then, PAH (0.4 g, after grinding) was added to the dispersed Fe_3O_4 MNPs solution. The mixture was dispersed for 2 h by ultrasonication. Under ultrasonication, the temperature was slowly (during 20 min) raised to 50°C and stirred for 28 h at this temperature. Then, the resulting nanocomposite, Fe_3O_4@PAH, was magnetically separated from solution, washed with 100 mL of water and dried in vacuum at 50°C (Figure 1).

Adsorption Measurement

The adsorption properties of the prepared Fe_3O_4@PAH nanocomposite for Pb^{2+} and Cd^{2+} were measured in batch experiments. We studied the effect of pH (1.0−6.0), kinetics time (5−90 min), temperature (298–328 K) and adsorption isotherms (initial concentration 0.05–150 mg L^{-1}) of the studied metal ions. We also investigated the effects of alkaline/earth metal ion concentrations (0−0.3 mol L^{-1}). Analyzing adsorption behavior of the Fe_3O_4@PAH nanocomposite involved adding 0.020 g of Fe_3O_4@PAH to 50 mL of solution of each metal ion at different concentrations at room temperature. The mass of the adsorbent was kept as 0.02 g, because it was minimum mass that can be separated from solution quantitatively. The pH was maintained at a constant value during adsorption. The equilibrium time was less than 1 h. When the adsorption behavior reached equilibrium, the adsorbents were separated by powerful magnets. The concentrations of the studied heavy metal ions in aqueous phase were determined using a Perkin-Elmer 2380-Waltham flame atomic absorption spectrophotometer (FAAS). Metal ion concentrations adsorbed per unit mass of the Fe_3O_4@PAH nanocomposite (mg metal ion per g dry Fe_3O_4@PAH) were calculated by using eq. (1). Removal efficiencies (%Re) were calculated by using eq. (2).

$$q_e = \frac{(C_0 - C_e) \times v}{m \times 1000} \quad (1)$$

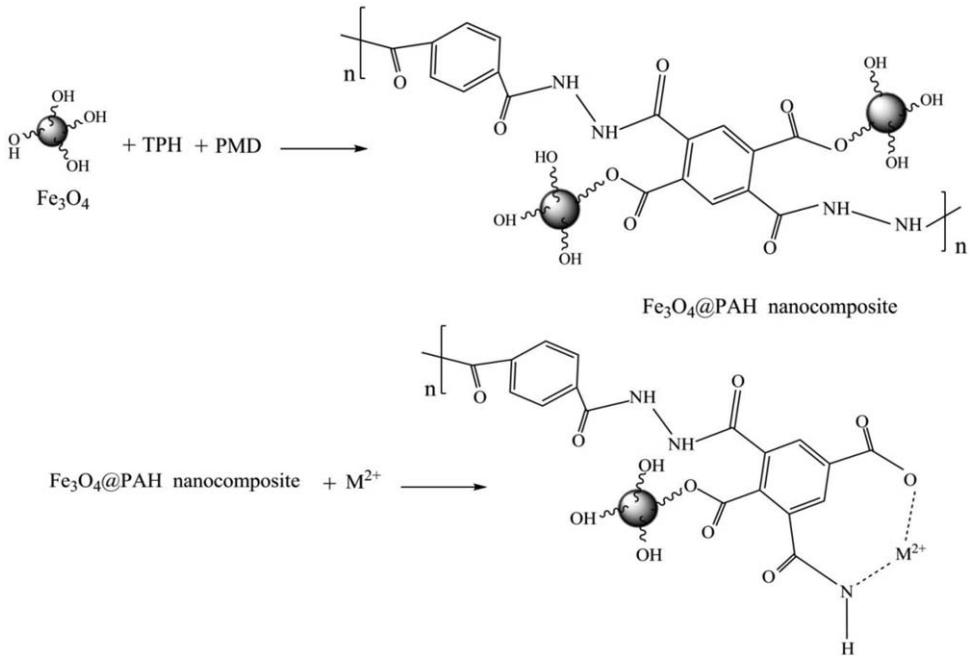

Figure 1. Schematic steps for the preparation of Fe_3O_4@PAH nanocomposite and a possible mechanism for adsorption of heavy metal ions by this system.

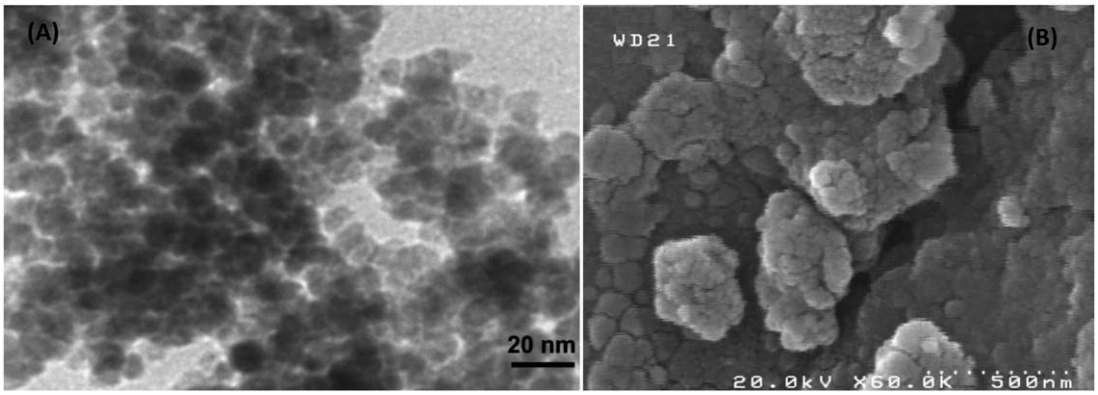

Figure 2. TEM image of the Fe_3O_4 MNPs (A) and SEM image of the Fe_3O_4@PAH nanocomposite (B).

$$\text{Removal}\% = \frac{(C_0 - C_e)}{C^0} \times 100 \quad (2)$$

In these equations, C_0 and C_e are the concentrations (mg L^{-1}) of the metal ions in the solution before and after the adsorption process, respectively; v is the volume of the solution (mL) and m is the mass of the adsorbent used (g).

Recovery and Reuse

To examine the possibility of the adsorbed metal ion recovery from the Fe_3O_4@PAH adsorbent, 0.02 g of the metal ion loaded Fe_3O_4@PAH adsorbent were stirred with HCl solution at room temperature for 3 h. The volume and concentration of the HCl solution were 10 mL and 0.2 mol L^{-1}, respectively. Then, the leached metal ion concentration in the solution was determined by FAAS. Due to decomposition effect of the strong alkaline solutions such as NaOH solutions on the polymeric structure of the adsorbent, after leaching the Fe_3O_4@PAH adsorbent were neutralized by 10 times washing with deionized water and again used in adsorption processes to investigate the reusability of the recovered adsorbent. Each Fe_3O_4@PAH adsorbent was used at least four times in the repeated adsorption−desorption cycles.

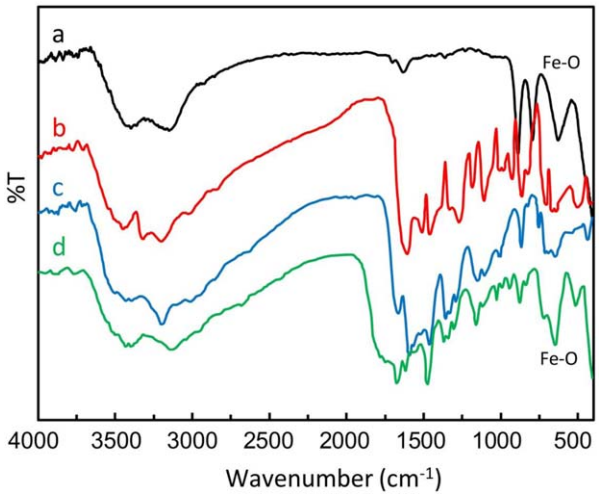

Figure 3. FT-IR spectra of the Fe_3O_4 (a), terephthalohydrazide (b), polyamic hydrazide (c), and Fe_3O_4@PAH (d). [Color figure can be viewed in the online issue, which is available at wileyonlinelibrary.com.]

RESULTS AND DISCUSSION

Characterization of the Prepared Materials

Figure 2 shows the TEM image of the obtained Fe_3O_4 nanoparticles and SEM image of the Fe_3O_4@PAH nanocomposite. As is clear from Figure 2(A), the diameters of the Fe_3O_4 nanoparticles are about 10−15 nm. Figure 2(B) shows that Fe_3O_4 nanoparticles have been covered with shells of PAH. According to BET measurements, the specific surface area of Fe_3O_4 nanoparticles and Fe_3O_4@PAH nanocomposite were 86.7 and 48.1 m^2 g^{-1}, respectively. Significant reduction in the surface area of the prepared Fe_3O_4@PAH nanocomposite confirms size enlargement of Fe_3O_4 particles during modification with PAH.

Also, the preparation of the Fe_3O_4@PAH nanocomposite was confirmed by FT-IR. The FT-IR spectra of the Fe_3O_4, TPH, PAH, and Fe_3O_4@PAH have been depicted in Figure 3(a−d), respectively. As is clear from Figure 3(a), peaks of 500−750 cm^{-1} belong to the Fe_3O_4.[22] As can be seen from Figure 3(b), presence of two peaks at 3209 and 3322 cm^{-1} (stretching vibration of NH_2 group) confirms the synthesis of TPH.

In addition, presence of a strong peak at 1641 cm^{-1} is clearly representative of carbonyl bond of hydrazone functional group. In Figure 4(c), two peaks at 3198 and 1705 cm^{-1} are ascribed to amide group (stretching vibration of N−H) and the carbonyl bond of carboxylic acid group, respectively. In addition,

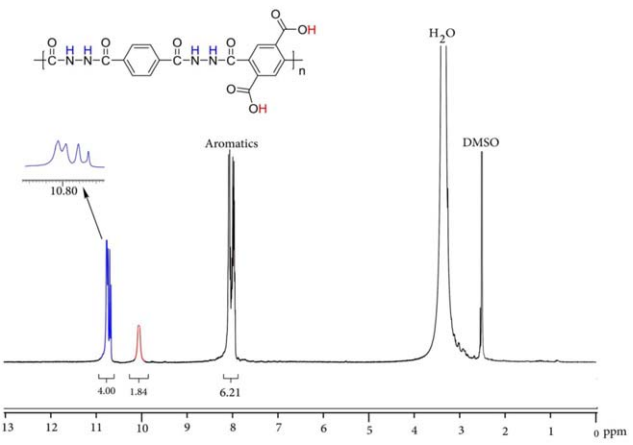

Figure 4. ^{1}H-NMR spectrum of PAH in DMSO. [Color figure can be viewed in the online issue, which is available at wileyonlinelibrary.com.]

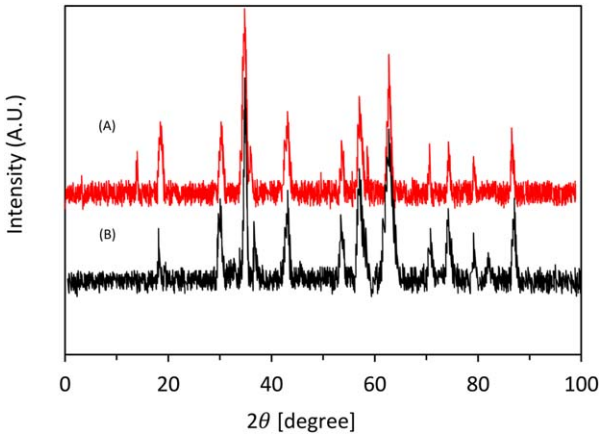

Figure 5. The XRD patterns of the synthesized Fe_3O_4 MNPs (a) and Fe_3O_4@PAH nanocomposite (b). [Color figure can be viewed in the online issue, which is available at wileyonlinelibrary.com.]

disappearance of two NH_2 peaks at 3209 and 3322 cm^{-1} clearly shows the synthesis of polymer. The similarity between Figure 3(c, d) spectra clearly confirms that PAH has been successfully bonded to the surface of Fe_3O_4 nanoparticles. In Figure 3(d), appearance of ester peak between 1730 and 1760 cm^{-1} demonstrated that polymer has been bonded to the surface of Fe_3O_4 nanoparticles via its carboxyl groups. Although hydrogen bonding and dipole–dipole interactions may contribute in PAH attachment to Fe_3O_4 nanoparticles.

For further structural confirmation of PAH, its ^{1}H-nuclear magnetic resonance (NMR) spectrum in DMSO is shown in Figure 4.

As is clear from Figure 4, peaks at 8, 10, and 10.8 ppm are ascribed to the protons of phenyl ring, protons of carboxylic acid groups, and protons of amide groups, respectively. It is immediately obvious that there is a satisfactory agreement between the positions of the recorded ^{1}H-NMR peaks and the expected positions for protons of PAH. Elemental analysis results showed that prepared polymer includes C (52.21%), N (13.34%), and H (2.98%). These results are in excellent agreement with calculated values for PAH: C (52.44%), N (13.59%), and H (2.93%). Furthermore, elemental analysis of the Fe_3O_4@-PAH nanocomposite showed that each gram of the nanocomposite includes 0.517 g of polymer.

The inherent viscositiy (η_{inh}) of the pure PAH was measured using 0.5 g/dL solution of it in DMSO at 30°C. The η_{inh} of the synthesized PAH was 0.57 ± 0.02 dL g^{-1}, which indicates relatively high molecular weight of the obtained polymer compared with previously reported hydrazide-based polymers.[21]

For phase confirmation of the prepared Fe_3O_4 nanoparticles, the XRD patterns of the Fe_3O_4 MNPs and Fe_3O_4@PAH were recorded. The results are shown in Figure 5. The reflection peak positions and relative intensities of the MNPs agree well with XRD patterns for Fe_3O_4 MNPs in the literature.[18,22] In addition, the XRD patterns of the Fe_3O_4 MNPs and Fe_3O_4@PAH nanocomposite have same peak positions, indicating that during nanocomposite preparation the phase of the Fe_3O_4 MNPs does not change.

Direct immobilization of PAH on the surface of the Fe_3O_4 nanoparticles poses significant advantage over the previously reported methods for modification of Fe_3O_4 nanoparticles.[16,17] Because, polyacrylic acid is not used in the modification of Fe_3O_4-PAH method, and hence the obtained Fe_3O_4 magnetic nanocomposite, Fe_3O_4@PAH is completely stable in water. Polyacrylic acid is soluble in water and hence, may cause some degree of instability in the structure of the prepared nanocomposite.

Adsorption Properties of the Prepared Fe_3O_4@PAH Nanocomposite for Pb^{2+} and Cd^{2+}

Effect of pH. Adjusting the pH of the metal ion solutions has significant effect on the removal efficiency of the Fe_3O_4@PAH adsorbent for Pb^{2+} and Cd^{2+} ions, because at low pH values (lower than 4) protonation of the nitrogen atoms of the active sites decreases the binding ability of the active sites toward metal ions. On the other hand, at pH values upper than 6, Pb^{2+} and Cd^{2+} may form hydroxide precipitates. Figure 6 demonstrates the influence of pH of test solution on the adsorption of Pb^{2+} and Cd^{2+} by Fe_3O_4@PAH nanocomposite at pH 1−6. As is clear from Figure 6, there are noteworthy increases in removal efficiency of the Pb^{2+} and Cd^{2+} ions with increasing pH values of the test solution from 1 to about 5. At pH values upper than 5, the removal efficiency value of Pb^{2+} is approximately constant, while removal efficiency value of Cd^{2+} moderately increases. To achieve optimum removal efficiency and prevent the risk of the hydroxide precipitation of the Pb^{2+} and Cd^{2+} ions, in the subsequent experiments, pH values of 5 and 6 were selected as the optimum values for the removal of Pb^{2+} and Cd^{2+}, respectively. The pH of the solutions was adjusted by the use of acetic acid/sodium acetate buffer. Industrial wastes (strongly acidic or basic solutions) were first neutralized with HCl or NaOH and then pH adjustments were accomplished by the use of acetic acid/sodium acetate buffer.

Adsorption Kinetics. In a practical point of view, adsorbents must have as high as possible adsorption rate to show usability in continuous systems. Figure 7 demonstrates the effects of time on the adsorption of the Pb^{2+} and Cd^{2+} by the Fe_3O_4@PAH adsorbent. As can be seen from Figure 7, the Pb^{2+} ions rapidly

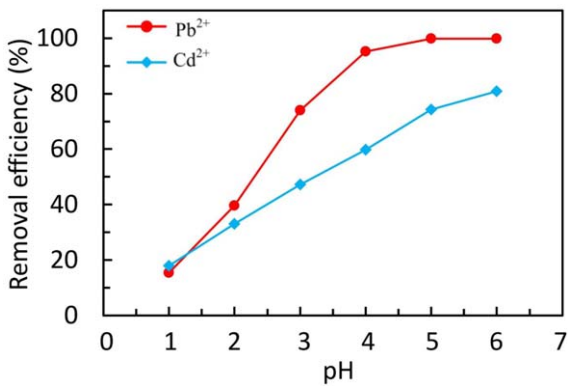

Figure 6. Effect of pH on the adsorption of Pb^{2+} and Cd^{2+}; adsorbent: 0.02 g, concentration of initial metal ions: 30 mg L^{-1}; volume of metal ions solution: 50 mL; time: 1 h, at 298 K. [Color figure can be viewed in the online issue, which is available at wileyonlinelibrary.com.]

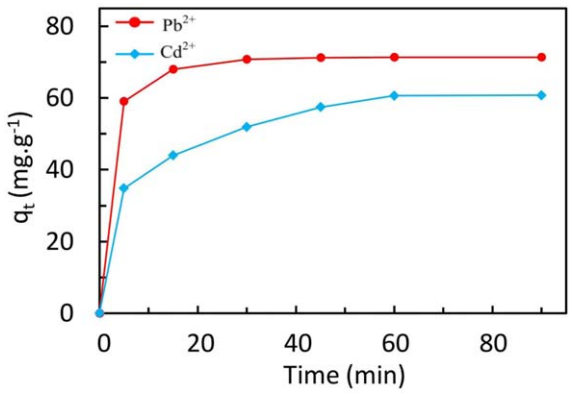

Figure 7. Effect of time on the adsorption of Pb^{2+} and Cd^{2+}; adsorbent: 0.02 g; concentration of metal ions: 30 mg L^{-1}; volume of test solution: 50 mL; pH: (5 for Pb^{2+} and 6 for Cd^{2+}); temperature: 298 K. [Color figure can be viewed in the online issue, which is available at wileyonlinelibrary.com.]

reached equilibrium in less than 30 min, while establishment of equilibrium for Cd^{2+} needs about 1 h. Compared with previously reported adsorbents, the Fe_3O_4@PAH nanocomposite has fast kinetics.[23,24] This fast adsorption could be attributed to the higher affinity of the amide and carboxylic acid active sites for complex formation with Pb^{2+} and Cd^{2+} as proposed in Figure 1.

Lagergren pseudo-first-order [eq. (3)] and pseudo-second-order [eq. (4)] models were used for further studying of the adsorption kinetics of Pb^{2+} and Cd^{2+} with PAH adsorbent:[25]

$$\ln(q_e - q_t) = \ln(q_e) - k_1 t \quad (3)$$

$$\frac{t}{q_t} = \left(\frac{1}{q_e}\right) t + \left(\frac{1}{k_2 \times q_e^2}\right) \quad (4)$$

In these equations q_t (mg g^{-1}) demonstrates the adsorption at time t (min); q_e (mg g^{-1}) shows the adsorption capacity at equilibrium time; k_1 (min^{-1}) is the rate constant for the pseudo-first-order model and k_2 (g mg^{-1} min^{-1}) is the rate constant for the pseudo-second-order model. The kinetic adsorption data were fitted to eqs. (3) and (4), and the obtained results were shown in Table I. As can be seen from Table I, the correlation coefficient (R) for the second-order kinetic model is about unity (0.99), which confirms the second-order nature of the adsorption of Pb^{2+} and Cd^{2+} ions on the surface of the Fe_3O_4@PAH adsorbent. This observation is in agreement with the complexation mechanism proposed in Figure 1 for adsorption of Pb^{2+} and Cd^{2+} ions by the Fe_3O_4@PAH adsorbent.[26]

Adsorption Isotherms of Fe_3O_4@PAH Adsorbent for Pb^{2+} and Cd^{2+}. Generally, the adsorption capacities of the adsorbents depend on the concentration of the adsorbate in solution, thus the effects of the solution concentration on the adsorption capacities of the Pb^{2+} and Cd^{2+} were investigated at optimum pH values (5 for Pb^{2+} and 6 for Cd^{2+}) and temperature 298 K. The mass of the Fe_3O_4@PAH adsorbent was 0.020 g and the concentration ranges were 0.5–150 and 5–150 mg L^{-1} for Pb^{2+} and Cd^{2+}, respectively. The contact times for Pb^{2+} and Cd^{2+} were 30 and 60 min, respectively. After equilibrium establishment between Fe_3O_4@PAH adsorbent and metal ion solution, the remained concentration of the metal ion in the solution was determined by using FAAS. Langmuir model [eq. (5)], Freundlich model [eq. (6)] and Temkin model [eq. (7)] were used for the analysis of the equilibrium isotherms for the adsorption of the Pb^{2+} and Cd^{2+} ions on the surface of the Fe_3O_4@PAH adsorbent:

$$\frac{C_e}{q_e} = \left(\frac{1}{q_{max}}\right) C_e + \left(\frac{1}{K_L \times q_{max}}\right) \quad (5)$$

$$q_e = K_F \times C_e^{(1/n)} \quad (6)$$

$$\theta = \frac{RT}{\Delta Q} \ln(k_T) + \frac{RT}{\Delta Q} \ln(C_e) \quad (7)$$

In these equations, q_e, C_e, q_{max}, K_L, K_F, and n are the adsorption capacity of Pb^{2+} and Cd^{2+} ions on the Fe_3O_4@PAH adsorbent (mg g^{-1}), the equilibrium ions concentration in solution (mg L^{-1}), the maximum capacity of the adsorbent (mg g^{-1}), the Langmuir adsorption constant (L mg^{-1}), the Freundlich constant (L mg^{-1}), and the heterogeneity factor, respectively.[27] In addition, θ, R, T, ΔQ, and k_T are the fractional coverage (q_e/q_{max}), the universal gas constant (kJ mol^{-1} K^{-1}), the temperature (K), the variation of adsorption energy (kJ mol^{-1}), and the Temkin equilibrium constant (L mg^{-1}), respectively.[28]

The results were depicted in Figure 8 and Table II. As is obvious from Figure 8 and Table II, the equilibrium capacities (q_e) of the Pb^{2+} and Cd^{2+} ions show remarkable enhancement with increasing the concentration of Pb^{2+} and Cd^{2+} in solution until reaching equilibrium. In addition, correlation coefficients (R) values for Langmuir model are higher than those of the Freundlich and Temkin model. These results indicate that adsorption isotherm data for Pb^{2+} and Cd^{2+} are clearly in better agreement with Langmuir model rather than Freundlich and Temkin model.

For further clarification of good agreement between experimental results and those results calculated from Langmuir model

Table I. Characteristics of the Applied Lagergren Pseudo-First-Order and Pseudo-Second-Order Kinetics Models for Adsorption of Pb^{2+} and Cd^{2+} by Fe_3O_4@PAH Nanocomposite

	2nd order			1st order			
Metal ions	R^2	q_e (mg g^{-1})	k_2	R^2	q_e (mg g^{-1})	k_1	q (mg g^{-1})[a]
Pb^{2+}	0.9999	71.9 ± 1.7	0.0244	0.8669	16.4 ± 2.2	0.0783	71.4 ± 2.3
Cd^{2+}	0.9934	62.8 ± 1.5	0.0038	0.8174	69.8 ± 6.3	0.0878	60.8 ± 2.4

q (mg g^{-1}) = $q_{experimental}$

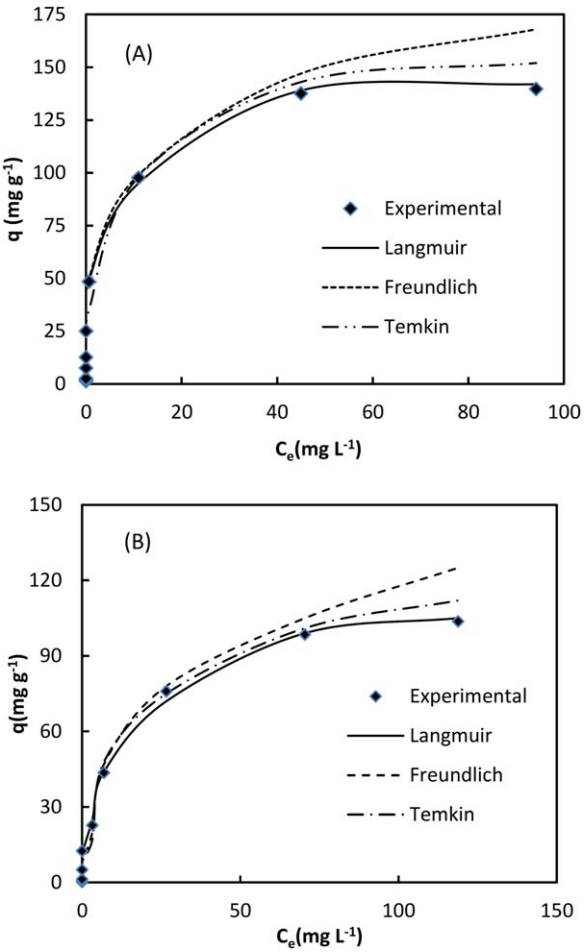

Figure 8. Equilibrium isotherms of Pb^{2+} and Cd^{2+} by Fe_3O_4@PAH nanocomposite, performed in batch mode; adsorbent: 0.02 g, initial concentration of metal ions: (0.5–150 mg L^{-1} for Pb^{2+} and 5–150 mg L^{-1} for Cd^{2+}); temperature: 298 K; pH: (5 for Pb^{2+} and 6 for Cd^{2+}); time: (30 min for Pb^{2+} and 60 min for Cd^{2+}). [Color figure can be viewed in the online issue, which is available at wileyonlinelibrary.com.]

and compare them with those obtained from Freundlich and Temkin model, a normalized deviation, $\Delta q_e\%$, was calculated using [eq. (8)]:[29]

$$\Delta q_e = \frac{\sum_{i=1}^{N} \left| \frac{(q_{e,i,\exp} - q_{e,i,\ cal})}{q_{e,i,\exp}} \right|}{N} \times 100 \qquad (8)$$

In eq. (8), $q_{e,\exp}$ and $q_{e,\mathrm{cal}}$ are amount of metal ions adsorbed experimental and calculated at equilibrium, respectively. N is number of measurements. The results were depicted in Table II. As is clear from Table II, the differences between experimental results and calculated results from Langmuir model is smaller than those obtained from Freundlich and Temkin model.

Appropriate fitness of the experimental results to Langmuir model indicates that Pb^{2+} and Cd^{2+} ions have been adsorbed as monolayer on the surface of the adsorbent particles. Again, this observation confirms our proposed mechanism for adsorption of Pb^{2+} and Cd^{2+} ions onto the Fe_3O_4@PAH particles via complex formation with donor sites of the Fe_3O_4@PAH adsorbent. As can be seen from Table II, the maximum capacity ($q_{\max}$) for Pb^{2+} and Cd^{2+} calculated by the Langmuir equation are 138.9 and 103.1 mg g^{-1}, respectively. The observed differences in the maximum capacities of Pb^{2+} and Cd^{2+} are most probably due to their different ability to interact with active sites of the Fe_3O_4@PAH adsorbent surface, Pb^{2+} ions have lower solvation energy than Cd^{2+} ions, thus they can more easily be released from solvent cages and interact with active sites of adsorbent.

As can be seen from Table II, the adsorption energy for Pb^{2+} and Cd^{2+} are −11.23 and −4.28 kJ mol^{-1}, respectively. These values were calculated from Temkin model. Negative adsorption energy may be due to bond formation between adsorbent functional groups and Pb^{2+} and Cd^{2+} metal ions, Negative adsorption energy, confirms our proposed mechanism for adsorption of Pb^{2+} and Cd^{2+} via complexation reaction between adsorbent sites and adsorbate. It must be noted that calculated adsorption energy values are equal to variation in enthalpy (ΔH) of adsorption, because adsorption process was performed at constant temperature and pressure.

To investigate the competitive adsorptions for mixture of Pb^{2+} and Cd^{2} ions, 0.020 g Fe_3O_4@PAH adsorbent was added to a solution (50 mL) containing equal initial concentrations (30 mg L^{-1}) of each metal ion. The pH was maintained at 5.2 and the equilibrium time was 60 min. After 60 min, the adsorbent particles were separated by powerful magnets and the removal efficiencies (*%Re*) were calculated by using the eq. (2). The obtained removal efficiencies for Pb^{2+} and Cd^{2+} were 98.3% and 74.7%, respectively. Again, these results confirm the higher ability of Pb^{2+} ions for interaction with active sites of Fe_3O_4@-PAH adsorbent.

Real samples such as industrial wastes include not only target pollutants but also possible interfering species, thus suitable adsorbents must be able to remove the target pollutants in the presence of coexisting interfering species. To examine the adsorptions characteristics of the target ions in the presence of possible interfering cations, 0.020 g Fe_3O_4@PAH adsorbent was

Table II. Langmuir, Freundlich, and Temkin Isotherm Model Constants and Correlation Coefficients for Adsorption of Pb^{2+} and Cd^{2+} by Fe_3O_4@PAH Nanocomposite

Model	Parameters	Pb^{2+}	Cd^{2+}
Langmuir	q_e (mg g^{-1})	71.6	62.4
	K_L (L mg^{-1})	1.44	0.742
	R^2	0.9977	0.9961
	$\Delta q_e\%$	0.23	0.34
Freundlich	K_F ($mg^{1-(1/n)}$ $L^{1/n}$ g^{-1})	14.125	4.689
	N	3.494	2.597
	R^2	0.1922	0.1677
	$\Delta q_e\%$	11.24	24.37
Temkin	ΔH (kJ mol^{-1})	−11.33	−4.28
	K_T (L mg^{-1})	0.260	0.713
	R^2	0.7433	0.6127
	$\Delta q_e\%$	7.34	9.16

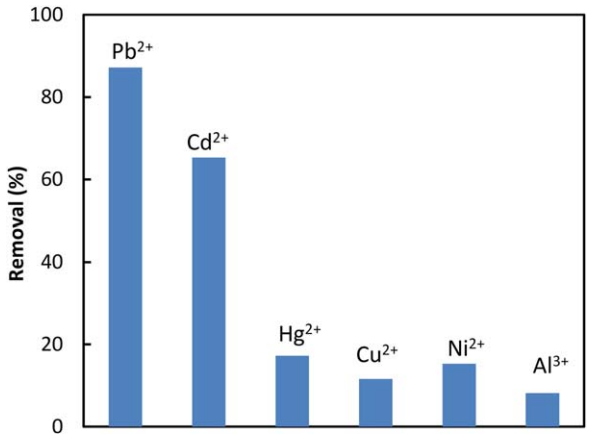

Figure 9. Competitive adsorption of different metal ions performed in batch mode; adsorbent: 0.02 g, initial concentration of metal ions: 30 mg L^{-1}, time: 60 min and pH: 5.2. [Color figure can be viewed in the online issue, which is available at wileyonlinelibrary.com.]

added to a solution (50 mL) containing equal initial concentrations (30 mg L^{-1}) of Pb^{2+}, Cd^{2+}, Hg^{2+}, Cu^{2+}, Ni^{2+}, and Al^{3+} ions. The pH of the solution was kept at 5.2 and the equilibrium time was selected as 60 min. After 60 min, the Fe_3O_4@-PAH particles were separated by a magnet and the removal efficiencies (%Re) of Pb^{2+} and Cd^{2+} in this mixture were calculated by using eq. (2). The results were depicted in Figure 9. As can be seen from Figure 9, the obtained removal efficiencies for Pb^{2+} and Cd^{2+} were 87.2% and 65.3%, respectively. These values are considerably higher than those of the other studied metal ions and confirm the selectivity of the proposed adsorbent for the removal of Pb^{2+} and Cd^{2+} in the presence of other coexisting cations. Good adsorption of Pb^{2+} and Cd^{2+} ions and weak adsorption of the other studied ions such as Hg^{2+}, Cu^{2+}, Ni^{2+}, and Al^{3+} may be due to soft–hard interactions between active sites of the adsorbent and metal ions. Among the studied cations, Pb^{2+} and Cd^{2+} have moderate degree of softness. On the other hand, the functional groups of the prepared nanocomposite are amide and amine. Amine and amide groups are known as moderate soft donors. Thus, the donor groups of the nanocomposite adsorbent have the best interaction with moderate soft acceptors such as Pb^{2+} and Cd^{2+}. Other studied ions are very soft acceptor or on the borderline of soft–hard acceptors, thus their interaction with active sites of the nanocomposite adsorbent is weak.

Table III compares the performance characteristics such as adsorption capacity, temperature, pH and dose of adsorbent for the prepared Fe_3O_4@PAH adsorbent with some of the previously reported adsorbents for Pb^{2+} and Cd^{2+} in the literature. As is clear from Table III, Fe_3O_4@PAH adsorbent shows remarkable enhancement in adsorption capacity for the removal of Pb^{2+} and Cd^{2+} over the previously reported adsorbents. High adsorption capacity of the prepared Fe_3O_4@PAH adsorbent together with its appropriate characteristics such as reusability, easy synthesis and easy separation make it suitable alternative to the well-known and widely used adsorbents for the removal of Pb^{2+} and Cd^{2+} from real samples such as industrial wastes and environmental waters.

Effect of Temperature on the Adsorption of Pb^{2+} and Cd^{2+}. To obtain proper removal efficiency some of the adsorbents must be used at special or limited range of temperature, this requirement imposes additional costs with special apparatus for maintaining temperature at a pre-defined level. The effects of the temperature on the adsorption capacities of Pb^{2+} and Cd^{2+} were studied under batch condition at optimum pH (5 for Pb^{2+} and 6 for Cd^{2+}) and time (30 min for Pb^{2+} and 60 min for Cd^{2+}). These experiments were carried out in five different temperatures (298, 308, 318, 328, and 338 K). The mass of the Fe_3O_4@PAH adsorbent was 0.020 g and the concentration ranges were 0.5–150 and 5–150 mg L^{-1} for Pb^{2+} and Cd^{2+}, respectively. After equilibrium establishment between Fe_3O_4@-PAH adsorbent and metal ion solution, the remained concentration of the metal ion in the solution was determined by using FAAS. Langmuir equation was used for calculation of the q_{max} values for each metal ion at different temperatures. The results are shown in Figure 10. As is obvious, increasing temperature until a temperature of about 328 K revealed no notable effect on the q_{max} values. In industrial applications, freedom of temperature changes is significant advantage for an adsorbent, because samples can be treated without any temperature

Table III. Comparison of Adsorption Characteristics of Different Adsorbents for the Removal of Pb^{2+} and Cd^{2+}

	Adsorption capacities (mg g^{-1})					
Type of adsorbent	Pb^{2+}	Cd^{2+}	pH	Temperature (°C)	Dose of adsorbent (g)	Reference
m-PAA-Na-coated MNPs	40	5	8	25	1	30
Amino-functionalized Fe_3O_4@SiO_2	76.6	-	6.2	45	0.02	31
Fe/Sn mixed-oxides	5.06	4.07	4-6	25	-	32
TiO_2 nanoparticles	-	7.9	9	25	0.02	33
Salicylic acid type chelate adsorbent	86.9	57.1	5	25	0.1	34
Carbon nanotube (MWCNTs)	97.08	10.86	5	-	0.05	35
Fe_3O_4@PAH nanocomposite	138.9	103.1	5-6	25	0.02	This work

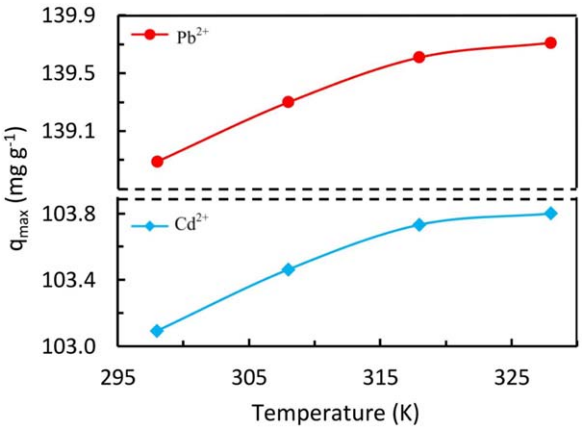

Figure 10. Effects of temperature on the maximum adsorption capacity (q_{max}) of the Fe_3O_4@PAH nanocomposite for adsorption of Pb^{2+} and Cd^{2+}, performed in batch mode; adsorbent: 0.02 g, initial concentration of metal ions: (0.5–150 mg L^{-1} for Pb^{2+} and 5–150 mg L^{-1} for Cd^{2+}); pH: (5 for Pb^{2+} and 6 for Cd^{2+}); time: (30 min for Pb^{2+} and 60 min for Cd^{2+}). [Color figure can be viewed in the online issue, which is available at wileyonlinelibrary.com.]

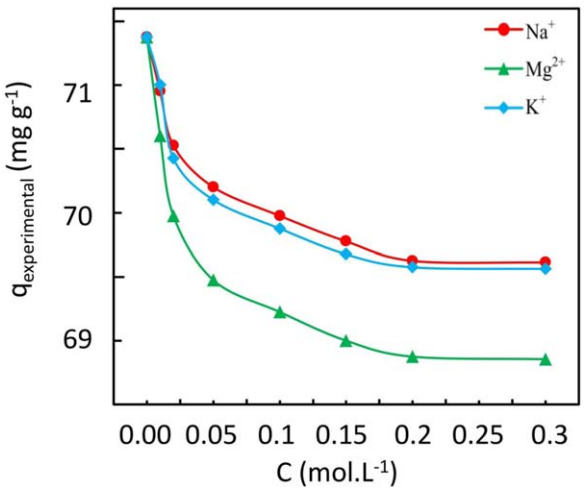

Figure 11. Effect of the alkaline/earth ions on the adsorption capacity of Fe_3O_4@PAH adsorbent for Pb^{2+}. [Color figure can be viewed in the online issue, which is available at wileyonlinelibrary.com.]

adjustments and, hence, does not need special apparatus for controlling the temperature.

Effect of Background Electrolytes. Usually, environmental samples such as groundwater and environmental waters have complex matrixes, for example, groundwater often contains considerable amounts of alkaline/earth metal ions. Therefore, an appropriate adsorbent must be able to remove heavy metal ions from samples in the presence of alkaline/earth metal ions. To investigate the applicability of the prepared Fe_3O_4@PAH adsorbent for the removal of target ions from environmental samples, the effects of the Na^+, K^+, and Mg^{2+} ions on adsorption capacity of Pb^{2+} were explored. As is obvious from Figure 11, the adsorption capacity of Pb^{2+} inconsiderably decreases (<3%) with addition alkaline/earth metal ions in a concentration range from 0.0 to 0.3 mol L^{-1}. The obtained results display that the proposed nanocomposite adsorbent can suitably remove the Pb^{2+} and Cd^{2+} ions from solution in the presence of considerable concentration of alkaline/earth metal ions. Again, the observed results confirm our proposed mechanism for the removal of Pb^{2+} and Cd^{2+} via complex formation with the donor sites of the Fe_3O_4@PAH adsorbent, accordingly Na^+, K^+, and Mg^{2+} cannot form complex species with polymer active sites and, hence, cannot be adsorbed on the Fe_3O_4@PAH adsorbent particles.

Desorption and Repeated Use

In practical applications, regeneration of adsorbents is an important issue, because can significantly reduce the cost of operations. Thus, the reusability of the prepared Fe_3O_4@PAH adsorbent was examined using the procedure described in "Recovery and Reuse", and the results are shown in Figure 12. As can be seen from Figure 12, the adsorption capacity of Fe_3O_4@PAH adsorbent for the removal of Pb^{2+} and Cd^{2+} is approximately constant for the four cycles, which shows that the complexation reaction between active sites of the Fe_3O_4@-PAH adsorbent and Pb^{2+} and Cd^{2+} ions is reversible. Reversibility of the adsorption reaction makes it possible to reuse the same Fe_3O_4@PAH adsorbent for several times for the removal of Pb^{2+} and Cd^{2+} from solution and, hence, reduce the overall cost of sample treatment.

Removal of Pb^{2+} and Cd^{2+} From Industrial Wastes

The practical utility of the prepared nanocomposite for the removal of Pb^{2+} and Cd^{2+} ions from real samples was evaluated using two different industrial wastes. Industrial wastes were collected (on June 2014) from Moham industrial complex (Iran, Isfahan) and Hesam paint producer company (Iran, Garmsar). The initial concentrations of Pb^{2+} and Cd^{2+} ions in the real samples were determined using a standard addition method and atomic absorption spectroscopy (AAS) detection. The remained concentration of Pb^{2+} and Cd^{2+} ions in the

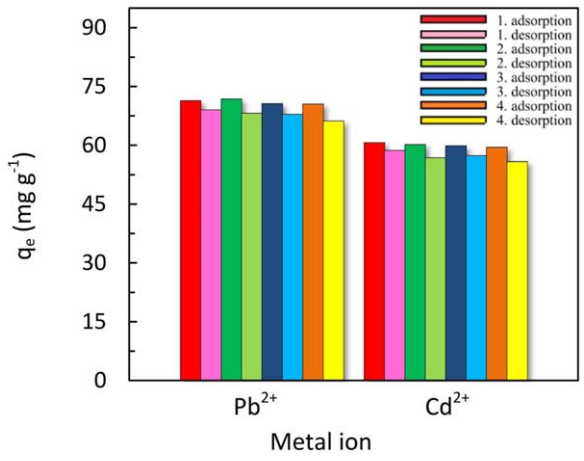

Figure 12. Performance of Fe_3O_4@PAH adsorbent by multiple regeneration cycles. [Color figure can be viewed in the online issue, which is available at wileyonlinelibrary.com.]

Table IV. Performance Characteristics of the Prepared Nanocomposite for the Removal of Pb^{2+} and Cd^{2+} from Industrial Wastes

Metal ions	Hesam paint company[a]		Moham industrial complex	
	Removal %	C_0 (mg L^{-1})	Removal %	C_0 (mg L^{-1})
Pb^{2+}	98.1 ± 3.6	332.8 ± 9.0	99.6 ± 2.5	1.8 ± 0.05
Cd^{2+}	88.3 ± 4.4	179.6 ± 7.1	96.8 ± 2.7	0.7 ± 0.03

[a] To use minimum amounts of nanocomposite, the adsorption–desorption cycles were repeated for Hesam paint producer company samples.

sample after treatment with adsorbent was determined AAS. The obtained results are shown in Table IV. Based on the obtained results, the Fe_3O_4@PAH adsorbent is able to quantitatively remove the Pb^{2+} and Cd^{2+} ions from real samples.

Mechanism Study

For polymer-based nanocomposites as adsorbents with large particle size, it is important to clarify the role of the intraparticle diffusion and external diffusion in the rate-controlling steps in the adsorption process. Normally Weber–Morris's Model [eq. (9)] and Boyd's diffusion model [eq. (10)] are used for investigating the rate-determining step in the adsorption process.[29,36]

$$q_t = k_{id}(t^{1/2}) + C \tag{9}$$

$$F = 1 - \left[\frac{6}{\pi^2}\right] \sum_{n=1}^{\infty} \left(\frac{1}{n^2}\right) \exp(-\pi^2 Bt) \tag{10}$$

In Weber–Morris's Model, q_t, k_{id}, t, and C are adsorption capacity (mg g^{-1}) at time t, the intraparticle diffusion rate constant (mg g^{-1} $min^{1/2}$), time (min), and the intercept, respectively.

In Boyd's diffusion model, F is the ratio of q_t to q_e at each time t and B is a constant. In the Weber–Morris's Model if the intraparticle diffusion is the rate-controlling step, then the plot of q_t versus $t^{1/2}$ will be linear and if the plot passes through the origin, then the rate will be controlled exclusively by intraparticle diffusion.[29] Presence of more than one linear segment in the plot of q_t versus $t^{1/2}$ implies that other physical phenomena along with intraparticle diffusion are involved in the rate-determining step. Figure 13 shows the plot of q_t versus $t^{1/2}$ for Pb^{2+} and Cd^{2+}. As is clear from Figure 13, both plots include two linear segments, confirming the presence of intraparticle diffusion together with other physical phenomena in the rate-controlling step.

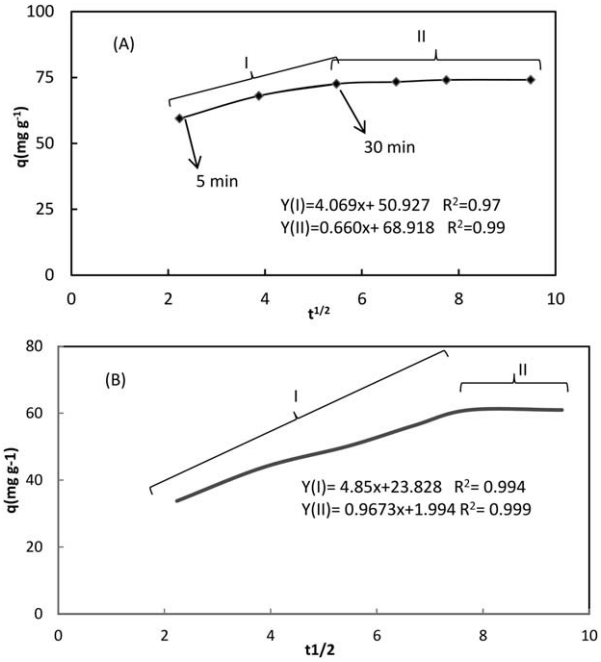

Figure 13. Plot of q_t versus $t^{1/2}$ for Pb^{2+} (A) and Cd^{2+} (B).

In Weber–Morris's Model, k_{id} can be obtained from slope of each linear segment in the plot of q_t versus $t^{1/2}$. In addition, intraparticle diffusivity D_i (cm min^{-1}) can be calculated from the following equation:

$$k_{id} = \left(\frac{3q_e}{dp}\right)\sqrt{\frac{D_i}{\pi}} \tag{11}$$

In eq. (11), dp (cm) is the particle diameter. The calculated parameters from Weber–Morris's Model are depicted in Table V. As can be seen from Table V, the calculated parameters from two linear segments in Figure 13 have different values. This effect may be due to the difference in the mass transfer rate for

Table V. Calculated Parameters from Weber–Morris' Diffusion Model for Adsorption of Pb^{2+} and Cd^{2+} by Fe_3O_4@PAH Nanocomposite

Calculated parameters from Weber–Morris' diffusion model for Pb^{2+}					
Based on the linear segment (I) in Figure 13(A)			Based on the linear segment (II) in Figure 13(A)		
K_I (mg g^{-1} min^{-1})	C_I (mg g^{-1})	D_I (cm^2 min^{-1})	K_{II} (mg g^{-1} min^{-1})	C_{II} (mg g^{-1})	D_{II} (cm^2 min^{-1})
4.07	50.93	2.21×10^{-5}	0. 66	68.92	5.81×10^{-7}

Calculated parameters from Weber–Morris' diffusion model for Cd^{2+}					
Based on the linear segment (I) in Figure 13(B)			Based on the linear segment (II) in Figure 13(B)		
K_I (mg g^{-1} min^{-1})	C_I (mg g^{-1})	D_I (cm^2 min^{-1})	K_{II} (mg g^{-1} min^{-1})	C_{II} (mg g^{-1})	D_{II} (cm^2 min^{-1})
4.85	23.83	4.63×10^{-5}	0. 967	1.99	1.84×10^{-6}

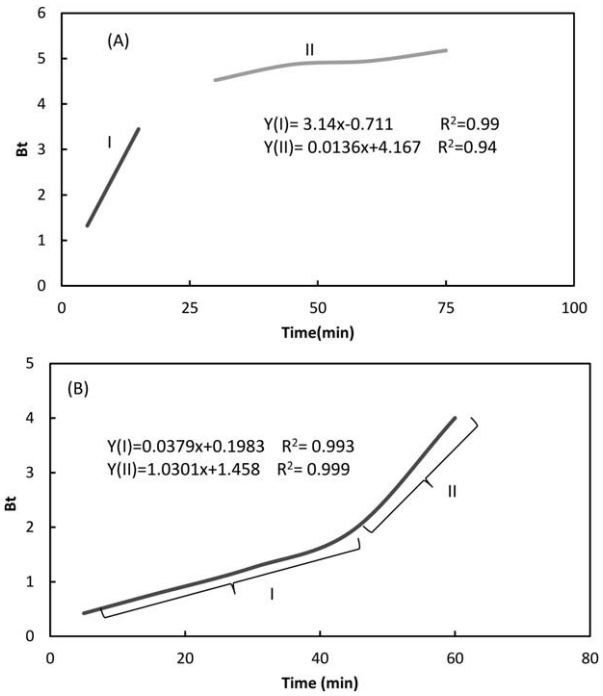

Figure 14. Boyd's plot for Pb^{2+}(A) and Cd^{2+} (B).

the initial and final stage of adsorption. This implies that diffusion into one class of pores was not the only rate limiting mechanism in the adsorption process.[29]

In Boyd's diffusion model, the term B_t can be calculated from eqs. (12) and (13):

$$F > 0.85 \quad B_t = -0.4977 - \ln(1-F) \tag{12}$$

$$F < 0.85 \quad B_t = \left(\sqrt{\pi} - \sqrt{(\pi - \frac{F\pi^2}{3})}\right)^2 \tag{13}$$

The Boyd's plot is then obtained by plotting B_t values versus time (t). If Boyd's plot is linear then it can be concluded that diffusion in pores is the rate determining step in the adsorption process. In this situation, B is equal to the slope of the linear plot. Then, the effective diffusion coefficient, D_i, ($cm^2\ s^{-1}$) can be obtained from eq. (14):

$$B = \left(\frac{D_i \pi^2}{d^2}\right) \tag{14}$$

In eq. (14), d (cm) is particle diameter. Figure 14 shows the Boyd's plot for adsorption of Pb^{2+} and Cd^{2+}. As is clear from Figure 14, both plots include two linear segments. In the Boyd's plot, each linear segment must be considered separately to obtain corresponding effective diffusion coefficient. In both plots, the segment that passes near the origin shows the intra pore diffusion stage. The segment that has greater intercept shows intraparticle diffusion. Table VI demonstrates the calculated parameters from Boyd's diffusion model for adsorption of Pb^{2+} and Cd^{2+} by Fe_3O_4@PAH nanocomposite. Again, it can be concluded that intraparticle diffusion is not an exclusive rate-determining step in the adsorption of Pb^{2+} and Cd^{2+} by Fe_3O_4@PAH nanocomposite.

CONCLUSIONS

In the first step of this work, terephthaloyl dichloride was synthesized from the reaction of terephthalic acid and thionyl chloride in dimethylformamide. In the second step, TPH was synthesized via the reaction of terephthaloyl dichloride and hydrazine hydrate. In the third step, a novel polymer PAH was synthesized via the reaction of TPH with PMD. The obtained PAH was characterized with NMR spectroscopy, FT-IR spectroscopy, and elemental analysis. In the fourth step, a novel magnetic nanocomposite was synthesized by immobilization of PAH on the Fe_3O_4 nanoparticles in water. In the fifth step, the applicability of the prepared Fe_3O_4@PAH nanocomposite for the removal of Pb^{2+} and Cd^{2+} ions from aqueous samples was investigated. Fe_3O_4@PAH nanocomposite showed notable selectivity for the removal of Pb^{2+} and Cd^{2+} ions in the presence of other heavy metal ions such as Hg^{2+}, Cu^{2+}, Ni^{2+}, Fe^{3+}, and Al^{3+}. The maximum adsorption capacities of Pb^{2+} and Cd^{2+} were found to be 138.9 and 103.1 mg g^{-1}, respectively. The adsorption capacities of the Fe_3O_4@PAH nanocomposite were free of temperature changes, thus it can be used for the removal of Pb^{2+} and Cd^{2+} from industrial wastes without adjusting the temperature of the samples. The Fe_3O_4@PAH nanocomposite was successfully used for the removal of Pb^{2+} and Cd^{2+} ions from industrial wastes.

Table VI. Calculated Parameters from Boyd's Diffusion Model for the Adsorption of Pb^{2+} and Cd^{2+} by Fe_3O_4@PAH Nanocomposite

Calculated parameters from Boyd's diffusion model for Pb^{2+}					
Based on the linear segment (I) in Figure 14(A)			Based on the linear segment (II) in Figure 14(A)		
B	Di_I ($cm^2\ min^{-1}$)	R^2	B	Di_I ($cm^2\ min^{-1}$)	R^2
3.14	6.69×10^{-3}	0.999	0.0136	2.90×10^{-5}	0.94

Calculated parameters from Boyd's diffusion model for Cd^{2+}					
Based on the linear segment (I) in Figure 14(B)			Based on the linear segment (II) in Figure 14(B)		
B	D_{iI} ($cm^2\ min^{-1}$)	R^2	B	D_i ($cm^2\ min^{-1}$)	R^2
0.0379	8.07×10^{-5}	0.992	1.301	2.77×10^{-3}	0.999

REFERENCES

1. Arvand, M.; Hassannezhad, M. *Mater. Sci. Eng. C* **2014**, *36*, 160.
2. Baghayeri, M.; Nazarzadeh Zare, E.; Lakouraj, M. M. *Biosens. Bioelectron.* **2014**, *55*, 259.
3. Afkhami, A.; Sayari, S.; Moosavi, R.; Madrakian, T. *J. Ind. Eng. Chem.* **2015**, *21*, 920.
4. Qiang, Z.; Bao, X.; Ben, W. *Water Res.* **2013**, *47*, 4107.
5. Bakhshayesh, S.; Dehghani, H. *Mater. Res. Bull.* **2013**, *48*, 2614.
6. Mangual, J. O.; Li, S.; Ploehn, H. J.; Ebner, A. D.; Ritter, J. A. *J. Magn. Magn. Mater.* **2010**, *322*, 3094.
7. Rezanejade Bardajee, G.; Hooshyar, Z.; Jahanbakhsh Asli, M.; Emamjome Shahidi, F.; Dianatnejad, N. *Mater. Sci. Eng. C* **2014**, *36*, 277.
8. Shete, P. B.; Patil, R. M.; Thorat, N. D.; Prasad, A.; Ningthoujam, R. S.; Ghosh, S. J.; Pawar, S. H. *Appl. Surf. Sci.* **2014**, *288*, 149.
9. Hasanabadi, N.; Ghaffarian, S. R.; Hasani-Sadrabadi, M. M. *Int. J. Hydrogen Energy* **2011**, *36*, 15323.
10. Gui, D.; Liu, C.; Chen, F.; Liu, J. *Appl. Surf. Sci.* **2014**, *307*, 172.
11. Zamani, F.; Hosseini, S. M. *Catal. Commun.* **2014**, *43*, 164.
12. Zamani, F.; Kianpour, S. *Catal. Commun.* **2014**, *45*, 1.
13. Bagheri, H.; Roostaie, A.; Baktash, M. Y. *Anal. Chim. Acta* **2014**, *816*, 1.
14. Salam, M. A.; El-Shishtawy, R. M.; Obaid, A. Y. *J. Ind. Eng. Chem.* **2014**, *20*, 3559.
15. Xu, P.; Zeng, G. M.; Huang, D. L.; Feng, C. L.; Hu, S.; Zhao, M. H.; La, C.; Wei, Z.; Huang, C.; Xie, G. X.; Liu, Z. F. *Sci. Total Environ.* **2012**, *424*, 1.
16. Zargoosh, K.; Abedini, H.; Abdolmaleki, A.; Molavian, M. R. *Ind. Eng. Chem. Res.* **2013**, *52*, 14944.
17. Zargoosh, K.; Zilouei, H.; Mohammadi, M. R.; Abedini, H. *Clean Soil Air Water* **2014**, *42*, 1.
18. Huang, S. H.; Chen, D. H. *J. Hazard. Mater.* **2009**, *163*, 174.
19. Liang, X.; Xu, Y.; Sun, G.; Wang, L.; Sun, Y.; Qin, X. *Colloids Surf. A* **2009**, *349*, 61.
20. Chen, W. J.; Tsai, P. J.; Chen, Y. C. *Anal. Chem.* **2008**, *80*, 9612.
21. Abdolmaleki, A. *Iran. Polym. J.* **2007**, *16*, 741.
22. Ge, F.; Li, M. M.; Ye, H.; Zhao, B. X. *J. Hazard. Mater.* **2012**, *211–212*, 366.
23. Nata, I. F.; Salim, G. W.; Lee, C. K. *J. Hazard. Mater.* **2010**, *183*, 853.
24. Peng, Q.; Liu, Y.; Zeng, G.; Xu, W.; Yang, C.; Zhang, J. *J. Hazard. Mater.* **2010**, *177*, 676.
25. Hao, Y. M.; Chen, M.; Hu, Z. *J. Hazard. Mater.* **2010**, *184*, 392.
26. Nabi, S. A.; Shahadat, M.; Shalla, A. H.; Khan, A. M. T. *Clean Soil Air Water* **2011**, *39*, 1120.
27. Shin, K.; Hong, J.; Jang, J. *J. Hazard. Mater.* **2011**, *190*, 36.
28. Hamdaoui, O.; Naffrechoux, E. *J. Hazard. Mater.* **2007**, *147*, 381.
29. Oliveira Sousa Neto, V.; Melo, D. Q.; de Oliveira, T. C.; Nonato, R.; Teixeira,P.; Silva, M. A. A.; do Nascimento, R. F. *J. Appl. Polym. Sci.* **2014**, *131*, 40744.
30. Mahdavian, A. R.; Mirrahimi, M. A. S. *Chem. Eng. J.* **2010**, *159*, 264.
31. Wang, J.; Zheng, S.; Shao, Y.; Liu, J.; Xu, Z.; Zhu, D. *J. Colloid Interf. Sci.* **2010**, *349*, 293.
32. Borai, E.; El-Sofany, E.; Morcos, T. *Adsorption* **2007**, *13*, 95.
33. Liang, P.; Shi, T.; Li, J. *Int. J. Environ. Anal. Chem.* **2004**, *84*, 315.
34. An, F.; Gao, B.; Dai, X. *J. Hazard. Mater.* **2011**, *192*, 956.
35. Li, Y. H.; Ding, J.; Luan, Z.; Di, Z.; Zhu, Y.; Xu, C.; Wei, B. *Carbon* **2003**, *41*, 2787.
36. Boyd, G. E.; Schubert, J.; Adamson, A. W. *J. Am. Chem. Soc.* **1947**, *69*, 2818.